

Review

Emerging Characterizing Techniques in the Fine Structure Observation of Metal Halide Perovskite Crystal

Kongchao Shen ^{1,2}, Jinping Hu ², Zhaofeng Liang ², Jinbang Hu ², Haoliang Sun ², Zheng Jiang ² and Fei Song ^{2,*} 

¹ Department of Physics, Zhejiang University, Hangzhou 310027, China; 11636007@zju.edu.cn

² Shanghai Institute of Applied Physics, Chinese Academy of Sciences, Shanghai 201204, China; hujinping@sinap.ac.cn (J.H.); liangzhaofeng@sinap.ac.cn (Z.L.); hujinbang@sinap.ac.cn (J.H.); sunhaoliang@sinap.ac.cn (H.S.); jiangzheng@sinap.ac.cn (Z.J.)

* Correspondence: songfei@sinap.ac.cn

Received: 30 March 2018; Accepted: 16 May 2018; Published: 23 May 2018



Abstract: Driven by its appealing application in the energy harvesting industry, metal halide perovskite solar cells are attracting increasing attention from various fields, such as chemistry, materials, physics, and energy-related industries. While the energy conversion efficiency of the perovskite solar cell is being investigated often by various research groups, the relationship between the surface structure and the property is still ambiguous and, therefore, becomes an urgent topic due to its wide application in the real environment. Recently, the fine structure characterization of perovskite crystals has been analysed by varying techniques, such as XRD, synchrotron-based grazing incidence XRD, XAFS, and STM, in addition to others. In this review article, we will summarize recent progresses in the monitoring of fine nanostructures of the surface and crystal structures of perovskite films, mainly by XAFS, XRD, and STM, focusing on the discussion of the relationship between the properties and the stability of perovskite solar cells. Furthermore, a prospective is given for the development of experimental approaches towards fine structure characterization.

Keywords: organic-inorganic crystal; surface structure; STM; calculation

1. Introduction

Metal halide perovskite structure has developed rapidly in the past decade since its first usage in solar cells. It is the champion of power conversion efficiency (PCE), increasing from 3.8% to more than 22% during recent years, while other types, such as Si-based, dye-sensitized, and organic solar cells, have had relatively less development in performance [1–4]. Perovskite films are commonly used in metal-halide solar cells with increasingly high PCE, however, the exact mechanism and the detailed structures of the perovskite film are still ambiguous. Consequently, much research has been performed on the stability [5–8], PCE [9,10], and toxicity [11,12] of the photosensitive film of the perovskite solar cell. In general, the perovskite solar cell is composed of the electrodes, electron transport layer, metal-halide perovskite film, and the hole transport layer. To reduce the influence of heterojunctions in solar cells, perovskite structures with single-crystal quality are a good candidate to detect related physic properties, such as giant photostriction [13], long range of electron-hole diffusion [14], structural and optoelectronic characteristics [15], harvesting of below-bandgap light absorption [16], optoelectronic properties [5], and ferroelectric and piezoelectric properties [17]. Moreover, perovskite crystals can also be utilized to detect related novel physical phenomenon, such as the quantification of re-absorption and re-emission processes, to determine photon recycling efficiency [18] and the detection of photons [19,20]. These investigations identifying such properties and physical phenomenon are performed in specific

perovskite crystals. Furthermore, high-performance single-crystal and planar-type photodetector has also been fabricated using single-crystal metal halide perovskite [21], as well as the narrow-band perovskite single-crystal photodetectors [22].

It has been acknowledged that perovskite crystals play an important role in the further promotion of perovskite solar cells' performance and industrial usage, as perovskite crystals have the distinct advantage of high controllability. Therefore, using perovskite crystals to solve one of the main issues of instability in perovskite solar cells might be reasonable. The subsequent question, then, is how to determine the crystal quality and characterize the fine structure, accordingly. Presently, there are several state-of-the-art techniques to achieve the structure determination of perovskite crystals, which will, therefore, be discussed and summarized in this review paper. First, we briefly summarize the growth methods of perovskite crystals with considerable discussion on the quality of perovskite crystals, which are investigated mainly by XRD, GIXRD, and XAFS. This covers reports from the literature, in addition to our own work. Secondly, the surface structures of perovskite crystals are investigated by scanning tunneling microscopy (STM) and are analyzed and compared with reports from the literature. The advantage of STM is that it gives a direct morphology of the perovskite surface with angstrom resolution in real space.

2. Basic Structure of Perovskite Crystals

Before discussing the approaches of growth of single crystal perovskite, it is worth noting the unit cell of perovskite crystal structure (molecular formula: ABX_3 , as depicted in Figure 1a). There are eight octahedral in one unit cell, where the cation, B, fits into an enclosed octahedral and the cation, A, is situated between the eight octahedral. The stability of the ABX_3 perovskite crystal structure can be determined by the tolerance factor (t), the range of which can be calculated by the formula (1) as shown below, where r_A , r_B , and r_X represent the corresponding ionic radii of the ABX_3 perovskite [23,24]. The site, A, usually represents the organic group (such as $CH_3NH_3^+$, $NH_2CH_2NH_3^+$, $C(NH_2)_3^+$, or Cs^+). The cation, B, is typically Pb^{2+} or Sn^{2+} , while the anion, X, is the halide ion (Cl^- , Br^- , or I^-). Furthermore, the cation, B, can also be easily connected with the anion, X, to form the BX_6 octahedral ionic group [25]. In Figure 1b, tolerance factors of perovskite crystal structures are listed and, subsequently, we can conclude that the ideal tolerance factor is from 0.9 to 1.0. The t range, from 0.7 to 0.9, can also represent the crystal structure because of the smaller A or large B in the ABX_3 structure. If the factor t is larger than 1.0, this means that there may exist various layered crystal structures. In addition, the Goldschmidt tolerance factor (t) and octahedral factor (μ) are also necessary, and these two factors can also be used to predict the formability of perovskites [26–28].

$$t = \frac{r_A + r_X}{\sqrt{2}(r_B + r_X)} \quad (1)$$

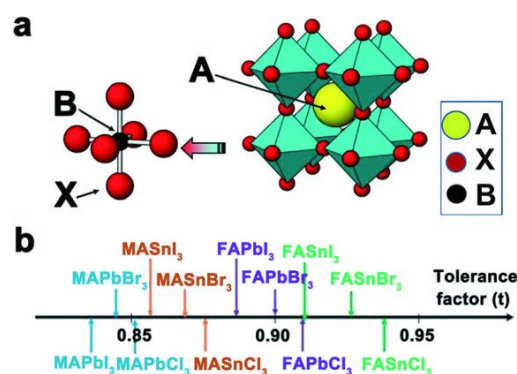


Figure 1. (a) Unit cell of ABX_3 with octahedral structure; (b) the tolerance factor of different crystal structures. Image is reproduced from Reference [24] with permission.

Apart from the phase (known as the α phase) of the perovskite structure shown in Figure 1, the crystal structure will also change in different temperature regions [23], such as the tetragonal phase (denoted as the β phase) and the orthorhombic phase (denoted as the γ phase) [29]. Accordingly, the phase transition in perovskite crystal structure can significantly alter its optical and electrical properties and, therefore, affect its applications significantly. In general, the most representative perovskite structure is MAPbI_3 , and its phase change is summarized in Figure 2 [30]. Starting from the transitional point of phase change at around 330 K, the cubic perovskite structure changes into the tetragonal phase along with the point group from $Pm-3m$ to $I4/mcm$. Contrastingly, the tetragonal changes into the orthorhombic phase, along with the structure phase evolution, from $I4/mcm$ to $P4/mbm$ when the temperature point drops below 160 K. Moreover, size-dependent orthorhombic-to-tetragonal phase transition has also been discovered by Li et al. [31]. Meanwhile, $\text{FA}_x\text{MA}_{1-x}\text{PbI}_3$ phase transition was discovered by Weber et al. [32]. It has been discovered that CsPbI_3 has two phases, α and δ , with the transition point at a temperature of approximately 600 K [33].

When single-crystal perovskite is exposed to ambient air dramatic changes occur, such as anisotropic moisture erosion of $\text{CH}_3\text{NH}_3\text{PbI}_3$ single crystals [34], and it can be estimated that the corresponding performance will be worsening over time [35]. The main explanation for this phenomenon is that the perovskite structure gets degraded and the crystal phase is destroyed by ambient molecules, which is confirmed by the observation of the color change in the appearance. Despite the structural degradation of perovskite crystals being well reported, little is known about what exactly happens at the nanoscale level.

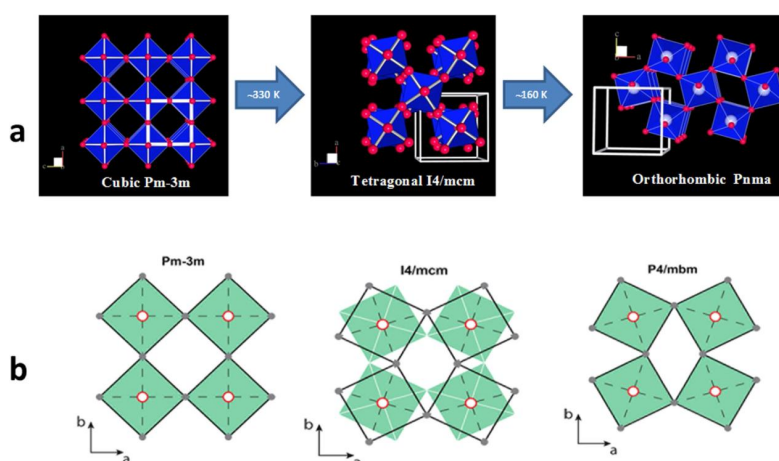


Figure 2. Crystal structures of MAPbI_3 at different temperatures. (a) The PbI_6 octahedra are blue and the iodine atoms are red, with MA cations not being shown to better highlight the distortions of the Pb-I network due to the structural phase transitions; (b) the relative rotations of neighboring layers of PbI_6 octahedra along the c axis are shown as filled green squares and unfilled black squares. Figures were taken from Reference [30] with permission.

Growth of ABX_3 Single Crystals

As discovered, the bottom-seeded solution growth (BSSG) method is suitable to grow perovskite crystals from materials in particular solvents, which have low solubility at room temperature, but increasing solubility as temperature rises. The first MAPbI_3 bulk single crystal with centimeter-scale was grown using this approach (as shown in Figure 3a) [36]. It was discovered that preparation conditions, such as temperature and crystal seed, are important to the growth of MAPbI_3 crystals. Figure 3a,b show different sizes of MAPbI_3 single crystals using the same method, except different temperature ranges are utilized (a with dimensions of 10 mm \times 10 mm \times 8 mm, and b with the size of 12 mm \times 12 mm \times 7 mm, respectively) [21,36]. Meanwhile, another similar method, top-seeded solution growth (TSSG), can produce MAPbI_3 single crystals with a size of 10 mm in length and 3.3 mm

in height, as shown in Figure 3c. [14] Using the same approach, $\text{CH}_3\text{NH}_3\text{SnI}_3$ and $\text{CH}(\text{NH}_2)_2\text{SnI}_3$ can also be obtained with a size of approximately 10 mm (Figure 3d,e) [37].

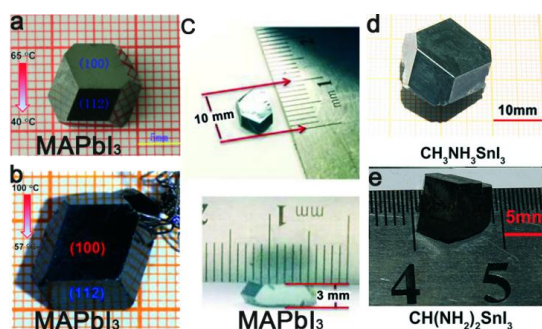


Figure 3. (a,b) Bottom seeded solution growth of MAPbI_3 single crystal perovskites with different temperature ranges resulting in different sizes; (c) Top seeded solution growth of MAPbI_3 single crystal; (d) MASnI_3 single crystal and (e) $\text{CH}(\text{NH}_2)_2\text{PbI}_3$ single crystal. The figure was taken from References [14,21,36,37] with permission.

Moreover, the temperature-lowering method is simple, convenient, and applicable for the growth of high quality single crystal perovskites with even larger sizes, such as MAPbX_3 ($X = \text{Cl}, \text{Br}, \text{I}$), MASnI_3 , and FASnI_3 . However, it is not suitable for low solubility materials and precursors at high temperatures. Compared with the temperature-lowering method, the inverse temperature crystallization (ITC) method is suitable for those materials whose solubility in particular solvents is high at room temperature but decreases with increasing temperature. By employing the ITC method, millimeter-sized MAPbX_3 ($X = \text{Cl}, \text{Br}, \text{I}$) single crystals were obtained via different organic solvents as shown in Figures 4a [38] and 4b [39]. Similarly, millimeter-size FAPbX_3 ($X = \text{Br}, \text{I}$) single crystals were gained using the same ITC method (Figure 4c) [40]. To some extent, residual molecules from the solvent can remain inside crystals. [41,42]

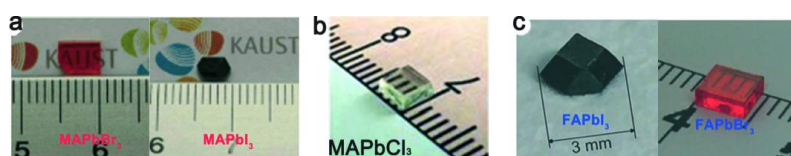


Figure 4. The inverse-temperature-crystallization method producing large-size crystals of (a) MAPbX_3 (b) MAPbCl_3 , and (c) FAPbX_3 . The figure was taken from refs [38–40] with permission.

The TSSP, BSSP, and ITC approaches are convenient to obtain single perovskite crystals and, therefore, has become the most widely used techniques in the laboratory. Despite this, other methods of growing perovskite crystals also exist. Firstly, millimeter-scale MAPbBr_3 crystals can be obtained by the anti-solvent vapor-assisted crystallization (AVC) method within one week [43], while single crystals (dimensions > 4 mm) were grown on the colorless $(\text{C}_6\text{H}_5\text{C}_2\text{H}_4\text{NH}_3)_2\text{PbCl}_4$ plate within several weeks [44]. Secondly, using the slow evaporation method, hybrid perovskite analogue (benzylammonium) $_2\text{PbX}_4$ ($X = \text{Cl}, \text{Br}$) crystals, with the dimensions of $5 \times 10 \times 2$ mm³, were obtained (Figure 5a) [45]. Thirdly, by using the droplet-pinned crystallization (DPC) measures, micrometer-scale single crystals $\text{CH}_3\text{NH}_3\text{PbI}_3$ were formed under a conventional, but efficient, preparation process, which also provided the possibility to grow single crystalline thin film (Figure 5b) [46]. Fourthly, using the combined solution process and the vapor-phase conversion method, 2D MAPbI_3 perovskite nanosheets were prepared via a twostep process by Liu et al. (Figure 5c) [47]. Last but not least, the hot casting method was also adopted for the growth of millimeter perovskite crystals [48].

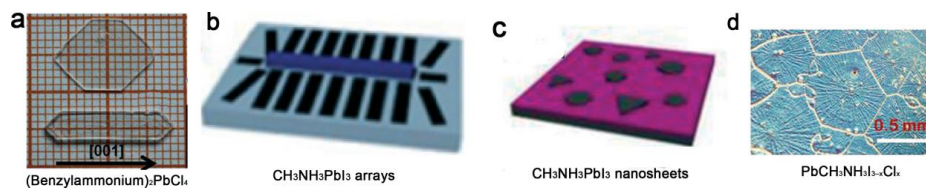


Figure 5. (a) Slow evaporation method produces the (benzylammonium)₂PbCl₄ perovskite single crystal; (b) Arrays of CH₃NH₃PbI₃ single crystal; (c) 2D MAPbI₃ perovskite nanosheets; (d) Milimeter-scale crystal grain [48]. The figure was taken from ref [45–48] with permission.

Presently, the most commonly used techniques for crystallization determination and fine structure exploitation are X-ray diffractions and other related measures, such as two-dimensional XRD (2DXRD) and grazing-incidence XRD. When the detecting area on the perovskite surface presents with single-crystal crystallization, patterns with short robs or dots will be seen in the 2D-XRD or GIXRD measurements, indicating the presence of a reciprocal lattice, as seen in Figure 6a [49]. In addition, we can also gather in-plane and out-of-plane information, as explained in Figure 6b,c. When polycrystalline orientation (Figure 6d) exists in the detecting area, a faint ring connecting short robs will be shown with a certain reciprocal space, q . Moreover, extra short robs also appear in the XRD pattern, which can be attributed to the formation of single crystals, but with different orientations. Compared to the pattern with short robs and faint rings, the complete ring presented in Figure 6e without short robs indicates that there are many single crystals with different orientations formed in the detected sample [50]. The difference between Figure 6d,e is the discrimination in growth methods, and it can be seen that the hot cast approach apparently improves the crystallinity of perovskite film and results in a better PCE.

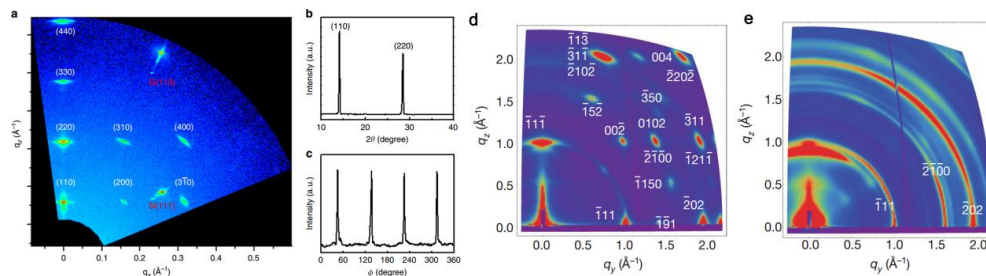


Figure 6. (a) 2D XRD of single-crystal patterned perovskite thin films prepared by the geometrically confined lateral crystal growth process; (b) Out-of-plane XRD scan. Diffraction peaks are consistent with the diffraction spots along the q_z line obtained by 2D XRD; (c) In-plane scan obtained at the fixed angle of (002) plane. The four sharp peaks demonstrate the four-fold symmetry of tetragonal perovskite; (d) Hot-cast and (e) near-single-crystalline (BA)₂(MA)₃Pb₄I₁₃ perovskite films with Miller indices of the most prominent peaks are shown. Color scale is proportional to the X-ray scattering intensity. The figure was taken from References [49,50] with permission.

While XRD gives the direct crystallization information of the perovskite structure, the fine structure inside perovskite crystals can also be determined by X-ray absorption fine structure spectroscopy (XAFS). This is achieved by fitting the raw data measured at the Pb L₃-edge, in the CH₃NH₃PbI_{3-x}Cl_x crystal, to get the information of the coordination number of Pb and the bonding length between Pb and I. Parameters obtained by fitting the Pb-L₃ EXAFS shows that there are vacancies and defects existing in this kind of perovskite crystal. Specifically, the multiple-shell fitting is better than the single-shell fitting, both in real space (R space) and reciprocal space (k space), as shown in Figure 7 [51]. Encouragingly, the XAFS approach can see more inside the perovskite crystal structure with complex unit cells, and get the atomic structure information, such as defects and so on.

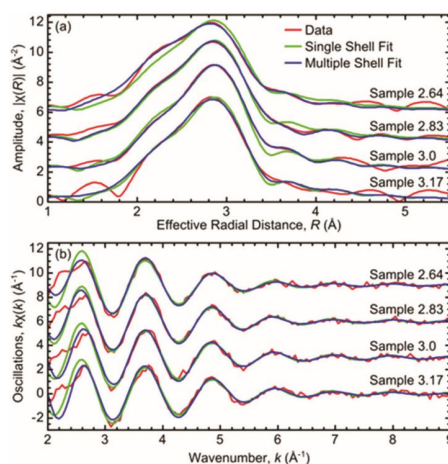


Figure 7. EXAFS spectra and fits in (a) R-space and (b) k-space for all samples. The figure was taken from Reference [51] with permission.

3. Surface Structure of ABX_3 Detecting by STM

Although ABX_3 perovskite crystals have been fabricated with a millimeter scale by using the different approaches discussed above, this is limited by the short lifetime of perovskite crystals in ambient atmosphere or the dirty crystal surface, and the surface morphology of perovskite crystals with atomic resolution was seldom mentioned. Initially, one method was proposed, with the codeposition of CH_3NH_3I and PbI_2 , to form $CH_3NH_3PbI_3$ followed by in-situ imaging with STM [52]. The (001) surface of the orthorhombic $MAPbI_3$ crystals were terminated either by MA-I or by Pb-I layers. As shown in Figure 8a–c, as the dimer and the zigzag structure are combined and potentially converted into each other at the (001) surface, the observed (001) surface by STM is, consequently, MA-I-terminated and bright protrusions in the STM images are assigned to iodine anions, due to the negligible contribution of electronic states near E_F from MA anions [53]. The detailed structure is shown in Figure 8d,e. Interestingly, all these results were supported by theoretical calculation. It is later discovered that the codeposition of PbI_2 and CH_3NH_3I is an ideal method for in-situ STM, and other measurements, in ultra-high vacuum (UHV). Koresh et al. suggested that the surface termination of the $CH_3NH_3PbBr_3$ (001) crystal surface is the methylammonium bromide (CH_3NH_3Br) layer, supported by angle resolved photoelectron spectroscopy (ARPES) and theoretical calculation [54]. The surface termination, together with the structural stability and electronic structures of $MAPbI_3$, that have been investigated so far are summarized in ref [55]. Haruyama et al. also reported the surface properties of $CH_3NH_3PbI_3$ perovskite crystals with STM and other UHV measurements [56], while the surface-related properties of $CH_3NH_3PbI_3$ perovskite thin film was also reported by Afzaal et al. [57].

Besides the growth of different kinds of ABX_3 perovskite crystals in UHV, cleaved surfaces from perovskite crystals have also been used in UHV. Interestingly, Márton Kollár presented a method which can guarantee the flat and clean surface of the $CH_3NH_3PbBr_3$ crystal and allows surface sensitive measurements, which is needed for the understanding and further engineering of this material family [58]. Furthermore, other in-situ cleave methods have also been used during STM experiments [59]. Ohmann et al. utilized in-situ cleaving of $CH_3NH_3PbBr_3$ crystal to exploit the molecular orientation on the perovskite surface. Exact orientation of the molecular dipole within the lattice, and especially the interplay of methylammonium (MA) groups with hosting anions detected by STM, shows that such perovskite crystals keeps the phenomenon of modified arrangements of atoms and molecules on the surface, and have structurally and electronically distinct domains with ferroelectric and antiferroelectric characteristics. All these behaviors can be explained by surface reconstruction and a substantial interplay of the orientations of the polar organic cations, $(CH_3NH_3)^+$, with the position of the hosting anions. The first observation of such surface reconstruction was very

similar to the report produced by Limin She [52]. As an example, two surface structures (zigzag and dimer) are shown in Figure 9a,c. Figure 9b,d are simulated STM images of the (010) plane of the orthorhombic crystal with surface reconstruction. The ferroelectric property of this kind of perovskite is different in various domains, as shown in Figure 9e. Meanwhile, we can also discover, from Figure 9f,g, the same defect, which was discussed and shown in Figure 8. In principle, STM measurements can reveal surface morphologies in real space with atomic resolution, as converted from measured electronic states and tunneling current. However, the limited-scale measurement (usually within micrometer) prevents the investigation of large-size perovskite crystals. Therefore, a complementary method to STM, such as angle resolved photoelectron spectroscopy (ARPES), will help to obtain the electronic structure in reciprocal space and the averaged information for large samples [54].

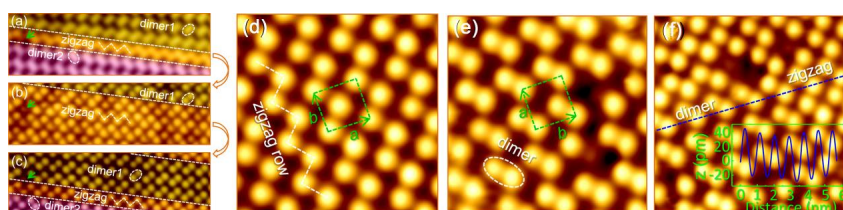


Figure 8. STM images of MAPbI₃ crystal films deposited on an Au(111) crystal surface. (a–c) Sequential images acquired at the same region showing the reversible transition between the dimer and zigzag structures ($4.2 \times 12.8 \text{ nm}^2$; $U = 2.0, 0.85, \text{ and } -1.25 \text{ V}$; $I = 30 \text{ pA}$). Phase boundaries are denoted by dotted lines. Iodine zigzag rows and dimers are denoted by dashed lines and ellipses, respectively; (d,e) Zoom-in view of the zigzag and dimer structures ($4.3 \times 4.3 \text{ nm}^2$; 2.5 V ; 50 pA). The unit cell is denoted by dashed rectangles; (f) STM image of the two phases coexisting at the same region ($5.6 \times 5.6 \text{ nm}^2$; $U = 2.5 \text{ V}$; $I = 50 \text{ pA}$). The inset is the height profile along the dashed line. The figure was taken from Reference [52] with permission.

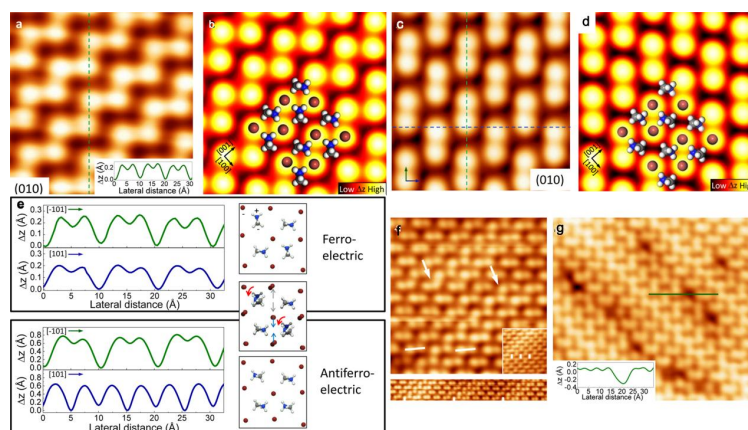


Figure 9. (a) Atomically resolved STM topography of the perovskite surface. Inset: Height profile along dashed line in the image. Image size: $31 \times 31 \text{ \AA}^2$ ($U = -5 \text{ V}$, $I = 0.1 \text{ nA}$); (b) Simulated STM image of the (010) plane of the orthorhombic crystal with surface reconstruction; (c) Image size: $31 \times 31 \text{ \AA}^2$ ($U = -9 \text{ V}$, $I = 0.1 \text{ nA}$); The arrows and dashed lines indicate the direction of the height profiles shown in part e; (d) Corresponding calculated image; (e) Comparison of height profiles and the corresponding model. The arrows indicate the rotational and positional change of the MA molecules and the Br ions, respectively, between the ferroelectric and antiferroelectric domain; (f) Start of the dislocation rows indicated by the white arrow. The angled lines indicate the modified Br atom positions adjacent to a dislocation row. Inset: Three dislocation rows beside each other. Bottom: Periodic arrangement of the dislocation rows; (g) STM image of defects on the surface. Image sizes: (f) $64 \times 64 \text{ \AA}^2$, inset $56 \times 55 \text{ \AA}^2$, bottom $164 \times 23 \text{ \AA}^2$; (g) $92 \times 103 \text{ \AA}^2$. $U = -9 \text{ V}$, $I = 0.1 \text{ nA}$. The figure was taken from Reference [59] with permission.

As discovered, both approaches of codeposition of PbI_2 and $\text{CH}_3\text{NH}_3\text{I}$, and cleaving from the pristine perovskite crystals cannot avoid surface defects, which have been resolved by STM. However, this raises the question of: how these defects will affect the physical properties of perovskite crystals. Liu et al. revealed the influence of defects in the crystal, as discussed in Figure 10 [60]. Vacancy sites, V_{Br} , V_{MA} , $V_{\text{Br-Pb}}$, and $V_{\text{Br-MA}}$, can be formed easily when water molecules are adsorbed on the (010) surface of the $\text{CH}_3\text{NH}_3\text{PbBr}_3$ perovskite crystal because water reduces the formation energy of vacancy sites. On the other hand, the pristine $\text{CH}_3\text{NH}_3\text{PbBr}_3$ (010) surface is shown to be quite inert toward the adsorption of molecules or atoms. Contrastingly, in the presence of vacancy sites, the adsorption energies of water, oxygen, and acetonitrile molecules are significantly increased due to the formation of hydrogen bonds between the adsorbates and the defective surface. It is expected that, in contrast to the pristine surface, structural decomposition of perovskite crystals is more likely to occur on the surface vacancy sites [60]. The stability of perovskite crystals or films is, therefore, very sensitive to water or other adsorbed molecules. In addition, polar solvents can also degrade the surface of perovskite crystals [61]. Dramatic changes, such as crystal structure and band gap, will appear on the surface of perovskite crystals after exposure to water, as suggested by Kamat et al. [62]. The formula of the chemical reaction between perovskite and water has been discussed in detail in ref. [7], however, oxygen is not the main contaminant. If the solar cells are stored in dark and dry air conditions, there will not be any noticeable degradation [63,64].

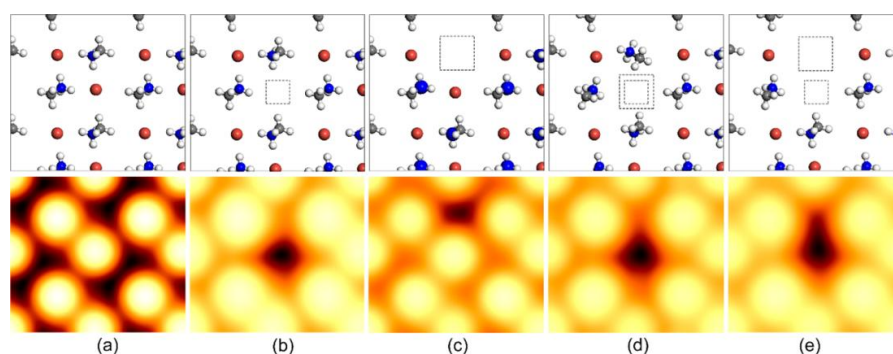


Figure 10. Simulated STM images of (a) the pristine $\text{CH}_3\text{NH}_3\text{PbBr}_3$ (010) surface and (b) the surface with a Br vacancy V_{Br} ; (c) a MA vacancy V_{MA} ; (d) a Br-Pb double vacancy $V_{\text{Br-Pb}}$; and (e) a Br-MA double vacancy $V_{\text{Br-MA}}$. All these STM images were calculated with a W(111) tip model. The squares show the position of missing Br, Pb atoms or MA cations. $V_{\text{bias}} = -3.0$ V. Color code: N (blue), C (gray), H (white), Br (brown). The figure was taken from Reference [60] with permission.

After the discussion of surface defects existing in perovskite crystal, which affects the stability of perovskite, the surface morphology of perovskite crystals exposed in ambient conditions will be discussed. The aged surfaces (from as-grown single crystals) of $\text{CH}_3\text{NH}_3\text{PbBr}_3$ are shown in Figure 11a,b, in which the period of the crystal can be seen clearly, while Figure 11c,d shows the surface structures of pristine crystals, which show 2D crystals or robs-like crystals. More detailed information is shown in Figure 11e,f with a magnified view. When the pristine surface was exposed in ambient conditions, the surface structure changed significantly, which originates from hydration-induced morphological changes. However, the reason that the water molecules cause surface structure restructuring is still unknown. Notably, surface reconstruction on aged surfaces (as visualized from atomic-scale scanning tunneling microscopy) might lead to changes in the composition and optical band gap, as well as the degradation of carrier dynamics, photocurrent, and solar cell device performance [65]. Additionally, ionic defects traveling through gaps between perovskite crystal grains to erode the perovskite's stability, as well as the band gap types (either direct or indirect band gap), will both influence the lifetime of charge carriers, the diffusion length, and the efficient absorption of perovskite semiconductors [66]. Therefore, a decreased grain boundary is favored for improving the

perovskite film's stability and the corresponding solar cell's performance, and a similar relativistic effect has also been reported using theoretical calculation [67–69].

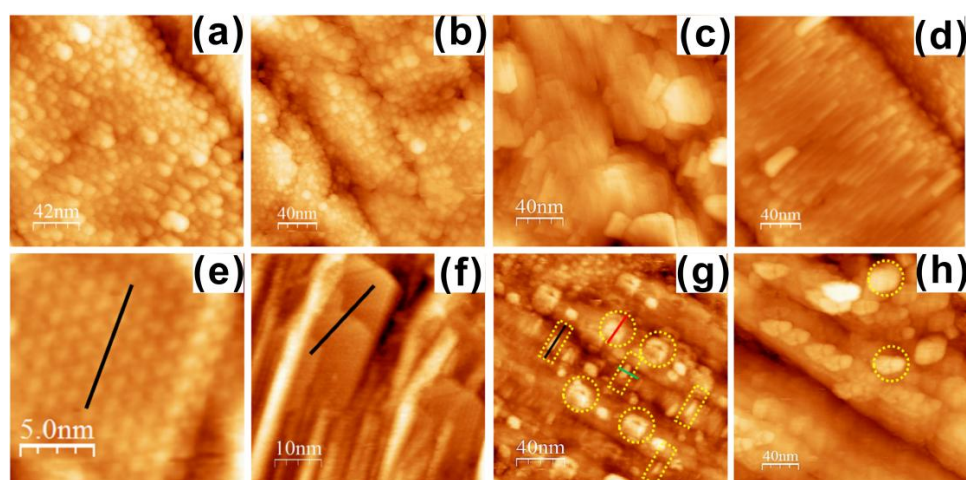


Figure 11. (a,b) STM image of the aged surface from the as-grown single crystal; (c,d) Magnified view at various positions from the pristine crystal; (e,f) Ordered structures having well-aligned stacked planes from the pristine perovskite crystal surface; (g,h) STM images showing the hydrate formation after overnight exposure to ambient air with ring-like protrusions (marked by circles) and the disordered 1D chain (marked by rectangles), indicating molecular water incorporation in the pristine surface. Scanning parameters: $V_b = 2.5$ V and $I_t = 0.7$ nA. The figure was taken from Reference [65] with permission.

The alignment of MA groups is theoretically predicted to play a decisive role in the structural and electronic properties of the perovskite, and the exact orientation of the MA ions on the surface has been precisely determined by STM. This is important for the development of stable perovskite materials. Promoting the development of perovskite solar cells toward their theoretical PCE requires delicate control over the charge carrier dynamics throughout the whole perovskite solar cell device. Based on a complementary understanding of the perovskite device's hybrid mechanism, the elaborate control over the carrier behavior in the perovskite film, especially across interfaces between different materials, is expected [70]. With better characterization of surface structures with XRD, STM, and so on, improved electronic properties of these materials could be gained by structure optimization from optimized growth methods, thus promoting device performance advantages. In pursuit of higher PCE, perovskite solar cells will definitely require an optimized carrier transport pathway, which is related to all device layers and corresponding interfaces. Presumably, flat perovskite crystal surfaces with less grain boundaries and stable surface structures will facilitate the charge extraction at both interfaces adjacent to the ETL, which is, essentially, helpful for obtaining a higher PCE. Moreover, atomic-scale defects can strongly influence the behavior of the solar cell absorber, and we have learned from the literature that the decomposition of perovskite crystal structures usually starts from surface defects. The identification of surface defects and their chemical properties should provide useful hints to understanding the chemical insights of the poor stability of $\text{CH}_3\text{NH}_3\text{PbX}_3$ perovskite crystals, which is the key origin of the device with high PCE but not long-term stability.

Based on these reports and investigations, a series of methods has, therefore, been proposed to improve the stability of perovskite films and crystals. For example, Long et al. report a high crystallized MAPbI_3 perovskite crystal with texture structure as prepared from HPbI_3 reacting with low partial pressure MA gas, which demonstrates substantially higher thermal and moisture stability compared to that of polycrystalline perovskite prepared from $\text{MAI} + \text{PbI}_2$ [8]. These observations suggest that the crystal-like perovskite sensitizer in solar cells possesses better performance than the three-dimensional (3D) perovskite structure, which can be utilized as an efficient approach to improve

the stability of perovskite crystals. Moreover, external doping with other organics or inorganics can also improve the stability of perovskite [70,71] crystals, as well as the coordination between the perovskite film and the adjacent film [72,73]. Nevertheless, stability is still one of the crucial issues in the development of perovskite solar cells. The 3D organic-inorganic perovskites are one of the most appealing thin-film solar-cell materials as they can absorb light over a broad range of solar spectrum wavelengths. However, a photovoltaic material needs to be stable for long periods when exposed to sunlight, and this is unfortunately not the case for 3D perovskites. Ruddlesden–Popper phases (layered 2D perovskite films) [50], on the other hand, are photostable, but only have a poor PCE, which is because organic cations in the material act as insulating spacing layers between the conducting inorganic slabs present and so inhibit charge transport in out-of-plane layers. Nevertheless, PCE is obviously another important factor for perovskite devices. Consequently, an ideal photovoltaic material should have both high PCE and long-term stability. Based on these requirements, 2D halide perovskites, formed on the 3D perovskite structure to passivate interfacial defects and vacancies, and enhance moisture tolerance, seems to be a promising approach. Interestingly, hybrid 3D/2D perovskite films possess longer photoluminescence lifetimes, as well as lower trap state densities by the passivation of cationic and halide vacancies on the surface or grain boundaries, thereby reducing the non-radiative recombination pathways. More importantly, the hybrid 3D/2D perovskite exhibits higher ambient stability than a pure 3D perovskite where the hydrophobic nature of the long aliphatic carbon chains in the 2D perovskite provide an additional moisture repelling effect to the entire perovskite film.

4. Overlook and Prospective

Typically, great crystallinity is essential to the performance of the perovskite solar cell. In this review paper, the fabrication of single-crystal perovskite structure has been briefly discussed, followed by the fine structure determination with XRD and GIXRD, which are the most common and efficient characterization methods, currently. Secondly, the surface properties of fabricated perovskite crystals, including termination layer, ferroelectric and anti-ferroelectric effects induced, surface defects, and stability, have been elaborately discussed, to reveal the relationship between surface defects and structure stability via STM at a nanoscale level, as well as the surface structure effect on the performance of perovskite solar cell. However, limited by the instability of the perovskite single-crystal structure, there is still a paucity of research investigating the single-crystal surface of the metal halo perovskite structure by STM.

As generally agreed, fine structure engineering is a key point to further improve the power conversion efficiency of perovskite solar cells. Consequently, substantial development of fine-structure characterization approaches will continually be a well-pursued topic in the field of organic-inorganic perovskite solar cells, especially in in-situ and operando conditions. X-ray fine structure absorption spectroscopy (XAFS) should be considerably employed in the future to characterize the detailed information behind crystal structure, such as the exact coordination information of metal ions in the hybridized perovskite structure (Pb, Cu, Sn, Cs, and so on), the bonding length, and the chemical state as-prepared and under operando situation. Moreover, atomic force microscopy (AFM) can also be widely utilized as a supplement to STM, which can measure the surface morphology in air or in situ. Scanning electron microscopy (SEM) has been widely used in the structure determination of perovskite films, however, its spatial resolution is still a limitation for fine structure characterization. Synchrotron-based scanning transmission electron microscopy can be a very helpful tool for both fine structure mapping and spatial element identification, which has not been mentioned in current literature. Besides XAFS, the promotion of other structure characterization methods under operando conditions is an appealing direction for research that should not be ignored. One possible way could be the combination of absorption spectroscopy and electrical measurements. Of course, X-ray photoelectron spectroscopy (XPS) together with ultraviolet photoelectron spectroscopy (UPS) are greatly helpful for the surface and interface electronic structure determination, such as the energy level

alignment, valence band structure, and core level state, which are closely connected to the electrical properties of perovskite solar cells.

Acknowledgments: This work is supported by National Natural Science Foundation (91545101, U1732267), The National Key Research and Development Program of China (2016YFA0401302) and The Hundred Talents Program of the Chinese Academy of Sciences.

Conflicts of Interest: The authors declare no conflicts of interest.

References

1. Kojima, A.; Teshima, K.; Shirai, Y.; Miyasaka, T. Organometal Halide Perovskites as Visible-Light Sensitizers for Photovoltaic Cells. *J. Am. Chem. Soc.* **2009**, *131*, 6050–6051. [[CrossRef](#)] [[PubMed](#)]
2. Kromdijk, J.; Glowacka, K.; Leonelli, L.; Gabilly, S.T.; Iwai, M.; Niyogi, K.K.; Long, S.P. Improving Photosynthesis and Crop Productivity by Accelerating Recovery From Photoprotection. *Science* **2016**, *354*, 857–861. [[CrossRef](#)] [[PubMed](#)]
3. Xu, Q.; Yuan, D.; Mu, H.; Igbari, F.; Bao, Q.; Liao, L. Efficiency Enhancement of Perovskite Solar Cells by Pumping Away the Solvent of Precursor Film Before Annealing. *Nanoscale Res. Lett.* **2016**, *11*, 248. [[CrossRef](#)] [[PubMed](#)]
4. Yang, S.; Fu, W.; Zhang, Z.; Chen, H.; Li, C. Recent Advances in Perovskite Solar Cells: Efficiency, Stability and Lead-Free Perovskite. *J. Mater. Chem. A* **2017**, *5*, 11462–11482. [[CrossRef](#)]
5. Li, W.; Rao, H.; Chen, B.; Wang, X.; Kuang, D. A Formamidinium-Methylammonium Lead Iodide Perovskite Single Crystal Exhibiting Exceptional Optoelectronic Properties and Long-Term Stability. *J. Mater. Chem. A* **2017**, *5*, 19431–19438. [[CrossRef](#)]
6. Asghar, M.I.; Zhang, J.; Wang, H.; Lund, P.D. Device Stability of Perovskite Solar Cells—A Review. *Renew. Sustain. Energy Rev.* **2017**, *77*, 131–146. [[CrossRef](#)]
7. Leijtens, T.; Eperon, G.E.; Noel, N.K.; Habisreutinger, S.N.; Petrozza, A.; Snaith, H.J. Stability of Metal Halide Perovskite Solar Cells. *Adv. Energy Mater.* **2015**, *5*, 1500963. [[CrossRef](#)]
8. Long, M.; Zhang, T.; Zhu, H.; Li, G.; Wang, F.; Guo, W.; Chai, Y.; Chen, W.; Li, Q.; Xu, J.; et al. Textured CH₃NH₃PbI₃ Thin Film with Enhanced Stability for High Performance Perovskite Solar Cells. *Nano Energy* **2017**, *33*, 485–496. [[CrossRef](#)]
9. Zhang, F.; Wang, Z.; Zhu, H.; Pellet, N.; Luo, J.; Yi, C.; Liu, X.; Liu, H.; Wang, S.; Xiao, Y.; et al. Over 20% PCE Perovskite Solar Cells with Superior Stability Achieved by Novel and Low-Cost Hole-Transporting Materials. *Nano Energy* **2017**, *41*, 469–475. [[CrossRef](#)]
10. Seok, S.I.; Grätzel, M.; Park, N. Methodologies Toward Highly Efficient Perovskite Solar Cells. *Small* **2018**, 1704177. [[CrossRef](#)] [[PubMed](#)]
11. Babayigit, A.; Ethirajan, A.; Muller, M.; Conings, B. Toxicity of Organometal Halide Perovskite Solar Cells. *Nat. Mater.* **2016**, *15*, 247–251. [[CrossRef](#)] [[PubMed](#)]
12. Giustino, F.; Snaith, H.J. Toward Lead-Free Perovskite Solar Cells. *ACS Energy Lett.* **2016**, *1*, 1233–1240. [[CrossRef](#)]
13. Zhou, Y.; You, L.; Wang, S.; Ku, Z.; Fan, H.; Schmidt, D.; Ruydy, A.; Chang, L.; Wang, L.; Chen, L.; et al. Giant Photostriction in Organic-Inorganic Lead Halide Perovskites. *Nat. Commun.* **2016**, *7*, 11193. [[CrossRef](#)] [[PubMed](#)]
14. Dong, Q.F.; Fang, Y.; Shao, Y.; Mulligan, P.; Qiu, J.; Cao, L.; Huang, J. Electron-Hole Diffusion Lengths > 175 nm in Solution-Grown CH₃NH₃PbI₃ Single Crystals. *Science* **2015**, *347*, 967–970. [[CrossRef](#)] [[PubMed](#)]
15. Park, N. Crystal Growth Engineering for High Efficiency Perovskite Solar Cells. *CrystEngComm* **2016**, *18*, 5977–5985. [[CrossRef](#)]
16. Chen, Z.; Dong, Q.; Liu, Y.; Bao, C.; Fang, Y.; Lin, Y.; Tang, S.; Wang, Q.; Xiao, X.; Deng, Y.; et al. Thin Single Crystal Perovskite Solar Cells to Harvest Below-Bandgap Light Absorption. *Nat. Commun.* **2017**, *8*, 1890. [[CrossRef](#)] [[PubMed](#)]
17. Ding, R.; Zhang, X.; Sun, X.W. Organometal Trihalide Perovskites with Intriguing Ferroelectric and Piezoelectric Properties. *Adv. Funct. Mater.* **2017**, *27*, 21. [[CrossRef](#)]

18. Fang, Y.; Wei, H.; Dong, Q.; Huang, J. Quantification of Re-Absorption and Re-Emission Processes to Determine Photon Recycling Efficiency in Perovskite Single Crystals. *Nat. Commun.* **2017**, *8*, 14417. [[CrossRef](#)] [[PubMed](#)]
19. Yakunin, S.; Dirin, D.N.; Shynkarenko, Y.; Morad, V.; Cherniukh, I.; Nazarenko, O.; Kreil, D.; Nauser, T.; Kovalenko, M.V. Detection of Gamma Photons Using Solution-Grown Single Crystals of Hybrid Lead Halide Perovskites. *Nat. Photonics* **2016**, *10*, 585–589. [[CrossRef](#)]
20. Dirin, D.N.; Cherniukh, I.; Yakunin, S.; Shynkarenko, Y.; Kovalenko, M.V. Solution-Grown CsPbBr₃ Perovskite Single Crystals for Photon Detection. *Chem. Mater.* **2016**, *28*, 8470–8474. [[CrossRef](#)] [[PubMed](#)]
21. Lian, Z.; Yan, Q.; Lv, Q.; Wang, Y.; Liu, L.; Zhang, L.; Pan, S.; Li, Q.; Wang, L.; Sun, J. High-Performance Planar-Type Photodetector On (100) Facet of MAPbI₃ Single Crystal. *Sci. Rep.* **2015**, *5*, 16563. [[CrossRef](#)] [[PubMed](#)]
22. Fang, Y.; Dong, Q.; Shao, Y.; Yuan, Y.; Huang, J. Highly Narrowband Perovskite Single-Crystal Photodetectors Enabled by Surface-Charge Recombination. *Nat. Photonics* **2015**, *9*, 679–686. [[CrossRef](#)]
23. Li, C.; Lu, X.; Ding, W.; Feng, L.; Gao, Y.; Guo, Z. Formability of ABX₃ (X = F, Cl, Br, I) Halide Perovskites. *Acta Crystallogr. B* **2008**, *64*, 702–707. [[CrossRef](#)] [[PubMed](#)]
24. Fan, Z.; Sun, K.; Wang, J. Perovskites for Photovoltaics: A Combined Review of Organic-Inorganic Halide Perovskites and Ferroelectric Oxide Perovskites. *J. Mater. Chem. A* **2015**, *3*, 18809–18828. [[CrossRef](#)]
25. Saidaminov, M.I.; Mohammed, O.F.; Bakr, O.M. Low-Dimensional-Networked Metal Halide Perovskites: The Next Big Thing. *ACS Energy Lett.* **2017**, *2*, 889–896. [[CrossRef](#)]
26. Li, C.; Soh, K.C.K.; Wu, P. Formability of ABO₃ Perovskites. *J. Alloys Compd.* **2004**, *372*, 40–48. [[CrossRef](#)]
27. Sun, Q.; Yin, W. Thermodynamic Stability Trend of Cubic Perovskites. *J. Am. Chem. Soc.* **2017**, *139*, 14905–14908. [[CrossRef](#)] [[PubMed](#)]
28. Li, Z.; Yang, M.; Park, J.S.; Wei, S.H.; Berry, J.J.; Zhu, K. Stabilizing Perovskite Structures by Tuning Tolerance Factor: Formation of Formamidinium and Cesium Lead Iodide Solid-State Alloys. *Chem. Mater.* **2016**, *28*, 284–292. [[CrossRef](#)]
29. Feng, J.; Xiao, B. Crystal Structures, Optical Properties, and Effective Mass Tensors of CH₃NH₃PbX₃ (X = I and Br) Phases Predicted from HSE06. *J. Phys. Chem. Lett.* **2014**, *5*, 1278–1282. [[CrossRef](#)] [[PubMed](#)]
30. Whitfield, P.S.; Herron, N.; Guise, W.E.; Page, K.; Cheng, Y.Q.; Milas, I.; Crawford, M.K. Structures, Phase Transitions and Tricritical Behavior of the Hybrid Perovskite Methyl Ammonium Lead Iodide. *Sci. Rep.* **2016**, *6*, 35685. [[CrossRef](#)] [[PubMed](#)]
31. Li, D.; Wang, G.; Cheng, H.; Chen, C.; Wu, H.; Liu, Y.; Huang, Y.; Duan, X. Size-Dependent Phase Transition in Methylammonium Lead Iodide Perovskite Microplate Crystals. *Nat. Commun.* **2016**, *7*, 11330. [[CrossRef](#)] [[PubMed](#)]
32. Weber, O.J.; Charles, B.; Weller, M.T. Phase Behaviour and Composition in the Formamidinium-Methylammonium Hybrid Lead Iodide Perovskite Solid Solution. *J. Mater. Chem. A* **2016**, *4*, 15375–15382. [[CrossRef](#)]
33. Dastidar, S.; Hawley, C.J.; Dillon, A.D.; Gutierrez-Perez, A.D.; Spanier, J.E.; Fafarman, A.T. Quantitative Phase-Change Thermodynamics and Metastability of Perovskite-Phase Cesium Lead Iodide. *J. Phys. Chem. Lett.* **2017**, *8*, 1278–1282. [[CrossRef](#)] [[PubMed](#)]
34. Lv, Q.; He, W.; Lian, Z.; Ding, J.; Li, Q.; Yan, Q. Anisotropic Moisture Erosion of CH₃NH₃PbI₃ Single Crystals. *Crystengcomm* **2017**, *19*, 901–904. [[CrossRef](#)]
35. Grancini, G.; D'Innocenzo, V.; Dohner, E.R.; Martino, N.; Srimath Kandada, A.R.; Mosconi, E.; De Angelis, F.; Karunadasa, H.I.; Hoke, E.T.; Petrozza, A. CH₃NH₃PbI₃ Perovskite Single Crystals: Surface Photophysics and their Interaction with the Environment. *Chem. Sci.* **2015**, *6*, 7305–7310. [[CrossRef](#)] [[PubMed](#)]
36. Dang, Y.; Liu, Y.; Sun, Y.; Yuan, D.; Liu, X.; Lu, W.; Liu, G.; Xia, H.; Tao, X. Bulk Crystal Growth of Hybrid Perovskite Material CH₃NH₃PbI₃. *Crystengcomm* **2015**, *17*, 665–670. [[CrossRef](#)]
37. Dang, Y.; Zhou, Y.; Liu, X.; Ju, D.; Xia, S.; Xia, H.; Tao, X. Formation of Hybrid Perovskite Tin Iodide Single Crystals by Top-Seeded Solution Growth. *Angew. Chem. Int. Ed.* **2016**, *55*, 3447–3450. [[CrossRef](#)] [[PubMed](#)]
38. Saidaminov, M.I.; Abdelhady, A.L.; Murali, B.; Alarousu, E.; Burlakov, V.M.; Peng, W.; Dursun, I.; Wang, L.; He, Y.; Goriely, A.; et al. High-Quality Bulk Hybrid Perovskite Single Crystals within Minutes by Inverse Temperature Crystallization. *Nat. Commun.* **2015**, *6*, 7586. [[CrossRef](#)] [[PubMed](#)]

39. Maculan, G.; Sheikh, A.D.; Abdelhady, A.L.; Saidaminov, M.I.; Haque, M.A.; Murali, B.; Alarousu, E.; Mohammed, O.F.; Wu, T.; Bakr, O.M. $\text{CH}_3\text{NH}_3\text{PbCl}_3$ Single Crystals: Inverse Temperature Crystallization and Visible-Blind UV-Photodetector. *J. Phys. Chem. Lett.* **2015**, *6*, 3781–3786. [[CrossRef](#)] [[PubMed](#)]
40. Saidaminov, M.I.; Abdelhady, A.L.; Maculan, G.; Bakr, O.M. Retrograde Solubility of Formamidinium and Methylammonium Lead Halide Perovskites Enabling Rapid Single Crystal Growth. *Chem. Commun.* **2015**, *51*, 17658–17661. [[CrossRef](#)] [[PubMed](#)]
41. Hao, F.; Stoumpos, C.C.; Liu, Z.; Chang, R.P.H.; Kanatzidis, M.G. Controllable Perovskite Crystallization at a Gas-Solid Interface for Hole Conductor-Free Solar Cells with Steady Power Conversion Efficiency Over 10%. *J. Am. Chem. Soc.* **2014**, *136*, 16411–16419. [[CrossRef](#)] [[PubMed](#)]
42. Guo, Y.; Shoyama, K.; Sato, W.; Matsuo, Y.; Inoue, K.; Harano, K.; Liu, C.; Tanaka, H.; Nakamura, E. Chemical Pathways Connecting Lead(II) Iodide and Perovskite via Polymeric Plumbate(II) Fiber. *J. Am. Chem. Soc.* **2015**, *137*, 15907–15914. [[CrossRef](#)] [[PubMed](#)]
43. Shi, D.; Adinolfi, V.; Comin, R.; Yuan, M.; Alarousu, E.; Buin, A.; Chen, Y.; Losovyj, Y. Solar Cells. Low Trap-State Density and Long Carrier Diffusion in Organolead Trihalide Perovskite Single Crystals. *Science* **2015**, *347*, 519–522. [[CrossRef](#)] [[PubMed](#)]
44. Mitzi, D.B. A Layered Solution Crystal Growth Technique and the Crystal Structure of $(\text{C}_6\text{H}_5\text{C}_2\text{NH}_3)_2\text{PbCl}_4$. *J. Solid State Chem.* **1999**, *145*, 694–704. [[CrossRef](#)]
45. Liao, W.; Zhang, Y.; Hu, C.; Mao, J.; Ye, H.; Li, P.; Huang, S.D.; Xiong, R. A Lead-Halide Perovskite Molecular Ferroelectric Semiconductor. *Nat. Commun.* **2015**, *6*, 7338. [[CrossRef](#)] [[PubMed](#)]
46. Ye, T.; Fu, W.; Wu, J.; Yu, Z.; Jin, X.; Chen, H.; Li, H. Single-Crystalline Lead Halide Perovskite Arrays for Solar Cells. *J. Mater. Chem. A* **2016**, *4*, 1214–1217. [[CrossRef](#)]
47. Liu, J.; Xue, Y.; Wang, Z.; Xu, Z.Q.; Zheng, C.; Weber, B.; Song, J.; Wang, Y.; Lu, Y.; Bao, Q.; et al. Two-Dimensional $\text{CH}_3\text{NH}_3\text{PbI}_3$ Perovskite: Synthesis and Optoelectronic Application. *ACS Nano* **2016**, *10*, 3536–3542. [[CrossRef](#)] [[PubMed](#)]
48. Nie, W.; Tsai, H.; Asadpour, R.; Blancon, J.C.; Neukirch, A.J.; Gupta, G.; Crochet, J.J.; Chhowalla, M.; Tretiak, S.; Wang, H.L.; et al. High-Efficiency Solution-Processed Perovskite Solar Cells with Millimeter-Scale Grains. *Science* **2015**, *347*, 522–525. [[CrossRef](#)] [[PubMed](#)]
49. Lee, L.; Baek, J.; Park, K.S.; Lee, Y.; Shrestha, N.K.; Sung, M.M. Wafer-Scale Single-Crystal Perovskite Patterned Thin Films Based On Geometrically-Confined Lateral Crystal Growth. *Nat. Commun.* **2017**, *8*, 15882. [[CrossRef](#)] [[PubMed](#)]
50. Tsai, H.; Nie, W.; Blancon, J.C.; Stoumpos, C.C.; Asadpour, R.; Harutyunyan, B.; Neukirch, A.J.; Verduzco, R.; Crochet, J.J.; Pedesseau, L.; et al. High-Efficiency Two-Dimensional Ruddlesden-Popper Perovskite Solar Cells. *Nature* **2016**, *536*, 312–316. [[CrossRef](#)] [[PubMed](#)]
51. McLeod, J.A.; Wu, Z.; Sun, B.; Liu, L. The Influence of the I/Cl Ratio on the Performance of $\text{CH}_3\text{NH}_3\text{PbI}_{3-x}\text{Cl}_x$ -based Solar Cells: Why is $\text{CH}_3\text{NH}_3\text{I}:\text{PbCl}_2=3:1$ the “Magic” Ratio? *Nanoscale* **2016**, *8*, 6361–6368. [[CrossRef](#)] [[PubMed](#)]
52. She, L.; Liu, M.; Zhong, D. Atomic Structures of $\text{CH}_3\text{NH}_3\text{PbI}_3$ (001) Surfaces. *ACS Nano* **2015**, *10*, 1126–1131. [[CrossRef](#)] [[PubMed](#)]
53. Wang, Y.; Gould, T.; Dobson, J.F.; Zhang, H.; Yang, H.; Yao, X.; Zhao, H. Density Functional Theory Analysis of Structural and Electronic Properties of Orthorhombic Perovskite $\text{CH}_3\text{NH}_3\text{PbI}_3$. *Phys. Chem. Chem. Phys.* **2013**, *16*, 1424–1429. [[CrossRef](#)] [[PubMed](#)]
54. Komesu, T.; Huang, X.; Paudel, T.R.; Losovyj, Y.B.; Zhang, X.; Schwier, E.F.; Zheng, M.; Iwasawa, H.; Shimada, K.; Saidaminov, M.I.; et al. Surface Electronic Structure of Hybrid Organo Lead Bromide Perovskite Single Crystals. *J. Phys. Chem. C* **2016**, *120*, 21710–21715. [[CrossRef](#)]
55. Haruyama, J.; Sodeyama, K.; Han, L.; Tateyama, Y. Termination Dependence of Tetragonal $\text{CH}_3\text{NH}_3\text{PbI}_3$ Surfaces for Perovskite Solar Cells. *J. Phys. Chem. Lett.* **2014**, *5*, 2903–2909. [[CrossRef](#)] [[PubMed](#)]
56. Haruyama, J.; Sodeyama, K.; Han, L.; Tateyama, Y. Surface Properties of $\text{CH}_3\text{NH}_3\text{PbI}_3$ for Perovskite Solar Cells. *Acc. Chem. Res.* **2016**, *49*, 554–561. [[CrossRef](#)] [[PubMed](#)]
57. Afzaal, M.; Salhi, B.; Al-Ahmed, A.; Yates, H.M.; Hakeem, A.S. Surface-Related Properties of Perovskite $\text{CH}_3\text{NH}_3\text{PbI}_3$ Thin Films by Aerosol-Assisted Chemical Vapour Deposition. *J. Mater. Chem. C* **2017**, *5*, 8366–8370. [[CrossRef](#)]

58. Kollár, M.; Ćirić, L.; Dil, J.H.; Weber, A.; Muff, S.; Ronnow, H.M.; Náfrádi, B.; Monnier, B.P.; Luterbacher, J.S.; Horváth, E.; et al. Clean, Cleaved Surfaces of the Photovoltaic Perovskite. *Sci. Rep.* **2017**, *7*, 695. [[CrossRef](#)] [[PubMed](#)]
59. Ohmann, R.; Ono, L.K.; Kim, H.; Lin, H.; Lee, M.V.; Li, Y.; Park, N.; Qi, Y. Real-Space Imaging of the Atomic Structure of Organic-Inorganic Perovskite. *J. Am. Chem. Soc.* **2015**, *137*, 16049–16054. [[CrossRef](#)] [[PubMed](#)]
60. Liu, Y.; Palotas, K.; Yuan, X.; Hou, T.; Lin, H.; Li, Y.; Lee, S. Atomistic Origins of Surface Defects in CH₃NH₃PbBr₃ Perovskite and their Electronic Structures. *ACS Nano* **2017**, *11*, 2060–2065. [[CrossRef](#)] [[PubMed](#)]
61. Suarez, B.; Gonzalez-Pedro, V.; Ripolles, T.S.; Sanchez, R.S.; Otero, L.; Mora-Sero, I. Recombination Study of Combined Halides (Cl, Br, I) Perovskite Solar Cells. *J. Phys. Chem. Lett.* **2014**, *5*, 1628–1635. [[CrossRef](#)] [[PubMed](#)]
62. Christians, J.A.; Miranda Herrera, P.A.; Kamat, P.V. Transformation of the Excited State and Photovoltaic Efficiency of CH₃NH₃PbI₃ Perovskite upon Controlled Exposure to Humidified Air. *J. Am. Chem. Soc.* **2015**, *137*, 1530–1538. [[CrossRef](#)] [[PubMed](#)]
63. Lee, M.M.; Teuscher, J.; Miyasaka, T.; Murakami, T.N.; Snaith, H.J. Efficient Hybrid Solar Cells Based On Meso-Superstructured Organometal Halide Perovskites. *Science* **2012**, *338*, 643–647. [[CrossRef](#)] [[PubMed](#)]
64. Kim, H.; Lee, C.R.; Im, J.H.; Lee, K.B.; Moehl, T.; Marchioro, A.; Moon, S.J.; Humphry-Baker, R.; Yum, J.H.; Grätzel, M.; et al. Lead Iodide Perovskite Sensitized All-Solid-State Submicron Thin Film Mesoscopic Solar Cell with Efficiency Exceeding 9%. *Sci. Rep.* **2012**, *2*, 591. [[CrossRef](#)] [[PubMed](#)]
65. Murali, B.; Dey, S.; Abdelhady, A.L.; Peng, W.; Alarousu, E.; Kirmani, A.R.; Cho, N.; Sarmah, S.P.; Parid, M.R.; Zhumekenov, A.A.; et al. Surface Restructuring of Hybrid Perovskite Crystals. *ACS Energy Lett.* **2016**, *1*, 1119–1126. [[CrossRef](#)]
66. Wang, T.; Daiber, B.; Frost, J.M.; Mann, S.A.; Garnett, E.C.; Walsh, A.; Ehrler, B. Indirect to Direct Bandgap Transition in Methylammonium Lead Halide Perovskite. *Energy Environ. Sci.* **2017**, *10*, 509–515. [[CrossRef](#)]
67. Zheng, F.; Tan, L.Z.; Liu, S.; Rappe, A.M. Rashba Spin-Orbit Coupling Enhanced Carrier Lifetime in CH₃NH₃PbI₃. *Nano Lett.* **2015**, *15*, 7794–7800. [[CrossRef](#)] [[PubMed](#)]
68. Kepenekian, M.; Robles, R.; Katan, C.; Saponi, D.; Pedesseau, L.; Even, J. Rashba and Dresselhaus Effects in Hybrid Organic-Inorganic Perovskites: From Basics to Devices. *ACS Nano* **2015**, *9*, 11557–11567. [[CrossRef](#)] [[PubMed](#)]
69. Etienne, T.; Mosconi, E.; De Angelis, F. Dynamical Origin of the Rashba Effect in Organohalide Lead Perovskites: A Key to Suppressed Carrier Recombination in Perovskite Solar Cells? *J. Phys. Chem. Lett.* **2016**, *7*, 1638–1645. [[CrossRef](#)] [[PubMed](#)]
70. Zhou, H.P.; Chen, Q.; Li, G.; Luo, S.; Song, T.B.; Duan, H.S.; Hong, Z.; You, J.; Liu, Y.; Yang, Y. Interface engineering of highly efficient perovskite solar cells. *Science* **2014**, *345*, 542–546. [[CrossRef](#)] [[PubMed](#)]
71. Li, X.; Guo, Y.; Luo, B. Improved Stability and Photoluminescence Yield of Mn²⁺-Doped CH₃NH₃PbCl₃ Perovskite Nanocrystals. *Crystals* **2018**, *8*, 4. [[CrossRef](#)]
72. Koh, C.W.; Heo, J.H.; Uddin, M.A.; Kwon, Y.; Choi, D.H.; Im, S.H.; Woo, H.Y. Enhanced Efficiency and Long-Term Stability of Perovskite Solar Cells by Synergistic Effect of Nonhygroscopic Doping in Conjugated Polymer-Based Hole-Transporting Layer. *ACS Appl. Mater. Interfaces* **2017**, *9*, 43846–43854. [[CrossRef](#)] [[PubMed](#)]
73. Yin, G.; Ma, J.; Jiang, H.; Li, J.; Yang, D.; Gao, F.; Zeng, J.; Liu, Z.; Liu, S.F. Enhancing Efficiency and Stability of Perovskite Solar Cells through Nb-Doping of TiO₂ at Low Temperature. *ACS Appl. Mater. Interfaces* **2017**, *9*, 10752–10758. [[CrossRef](#)] [[PubMed](#)]

